



1 **Arctic sea level variability from high-resolution model simula-**  
2 **tions and implications for the Arctic observing system**

3 Guokun Lyu<sup>1,2</sup>, Nuno Serra<sup>2</sup>, Meng Zhou<sup>1</sup>, and Detlef Stammer<sup>2</sup>

4 <sup>1</sup> School of Oceanography, Shanghai Jiao Tong University, Shanghai, 200030, China

5 <sup>2</sup> Center for Earth System Research and Sustainability (CEN), University of Hamburg, Hamburg, 20146, Ger-  
6 many

7 *Correspondence to:* Guokun Lyu ([guokun.lyu@sjtu.edu.cn](mailto:guokun.lyu@sjtu.edu.cn))



8 **Abstract.** Two high-resolution model simulations are used to investigate the spatio-temporal variability of the  
9 Arctic Ocean sea level. The model simulations reveal barotropic sea level variability at periods <30 days, which  
10 is strongly captured by bottom pressure observations. The seasonal sea level variability is driven by volume  
11 exchanges with the Pacific and Atlantic Oceans and the redistribution of the water by the wind. Halosteric ef-  
12 fects due to river runoff and evaporation minus precipitation (EmPmR), ice melting/formation also contribute in  
13 the marginal seas and seasonal sea ice extent regions. In the central Arctic Ocean, especially the Canadian Basin,  
14 the decadal halosteric effect dominates sea level variability. Satellite altimetric observations and Gravity Recov-  
15 ery and Climate Experiment (GRACE) measurements could be used to infer freshwater content changes in the  
16 Canadian Basin at periods longer than one year. The increasing number of profiles seems to capture freshwater  
17 content changes since 2007, encouraging further data synthesis work with a more complicated interpolation  
18 method. Further, in-situ hydrographic observations should be enhanced to reveal the freshwater budget and  
19 close the gaps between satellite altimetry and GRACE, especially in the marginal seas.



## 20 **1 Introduction**

21 The Arctic Ocean is experiencing pronounced changes (e.g., Perovich et al., 2020; AMAP, 2019). Observa-  
22 tions have revealed increased warm inflows through the Bering Strait (Woodgate et al., 2012) and the Fram  
23 Strait (Polyakov et al., 2017), and an unprecedented freshening of the Canadian Basin especially the Beaufort  
24 Gyre (Proshutinsky et al., 2019). The rapid changes potentially impact the weather and climate of the northern  
25 hemisphere (Overland et al., 2021).

26 As an integrated indicator, sea level change reflects changing ocean conditions caused by ocean dynamics,  
27 atmospheric forcing, and terrestrial processes (Stammer et al., 2013). Satellite altimetry, together with bottom  
28 pressure observations from Gravity Recovery and Climate Experiment (GRACE), has been applied to infer  
29 ocean temperature and salinity changes that are not measured directly in the Arctic Ocean (e.g., Armitage et al.,  
30 2016) and in the deep ocean (e.g., Llovel et al., 2014), enhancing our ability to monitor ocean changes.

31 Over the past decades, coupled ocean-sea ice models and observations have advanced our understanding of  
32 the Arctic Ocean variability. Proshutinsky and Johnson (1997) demonstrated wind-forced cyclonic/anticyclonic  
33 ocean circulation patterns accompanied by dome-shaped sea levels variation using a barotropic model simula-  
34 tion. Further, in the Canadian Basin, ocean circulation changes result in freshwater accumulation and releasing,  
35 very well correlated to sea level changes (Koldunov et al., 2014; Proshutinsky et al., 2002). Given that sea level  
36 changes reflect freshwater content changes in the Canadian Basin, Giles et al. (2012) and Morison et al. (2012)  
37 proposed to use satellite altimetry observations and GRACE observations to infer freshwater content changes.  
38 The method was then applied to explore the freshwater content changes in the Beaufort Gyre (Armitage et al.,  
39 2016; Proshutinsky et al., 2019) at seasonal to decadal timescales. In the Barents Sea, Volkov et al. (2013) used  
40 altimetric sea level observations and the ECCO reanalysis (Forget et al., 2015) to explore seasonal to interannual  
41 sea level anomalies, revealing different roles of mass-related changes, thermosteric and halosteric effects on  
42 different regions of the Barents Sea.

43 However, the sparseness of in-situ profiles, coarse resolution and significant uncertainties of satellite altim-  
44 etry and GRACE observations result in large gaps in understanding the spatio-temporal variability of the Arctic  
45 sea level and its relations to the thermo/halosteric effects and mass changes (Ludwigsen and Andersen, 2021).  
46 Previous studies mainly focus on the decadal sea level variability (e.g., Koldunov et al., 2014; Proshutinsky et al.,  
47 2007; Proshutinsky and Johnson, 1997), and no study has yet fully explored the Arctic sea level variability at  
48 different spectral bands, and its dependence on the mass component and the vertical oceanic variability. Such a  
49 study could help identify critical regions and environmental parameters that need to be coordinately observed  
50 and point out observational gaps that need to be filled in the future.

51 Our study systematically explores the Arctic sea level variability as function of timescale and geographic  
52 location using daily and monthly outputs of two high-resolution model simulations. Contributions from ba-  
53 rotropic changes expressed in bottom pressure variations and baroclinic processes represented by ther-  
54 mo/halosteric changes are quantified at different timescales. We further discuss the existing Arctic Ocean ob-  
55 serving system's capability to monitor the Arctic freshwater content variability.

56 The structure of the remaining paper is as follows: the numerical models and the observations from the bot-  
57 tom pressure sensor, GRACE, and satellite altimetry are described in Section 2, together with different compo-  
58 nents of sea level changes. We compare the model simulations against observations in Section 3. Section 4 ana-  
59 lyzes sea level variability and associated mechanisms at high frequency (<30 days), at the seasonal cycle and at



60 decadal timescales. The relations with bottom pressure and thermohalosteric components are demonstrated,  
61 pointing out key regions and parameters we need to observe. Further, we analyze the ability of satellite altimetry,  
62 GRACE, and the in situ profiler system to monitor the Arctic freshwater content variability in Section 5. Section  
63 6 provides a summary and conclusions.

## 64 2 Model Simulations and observations

### 65 2.1 Atlantic-Arctic simulations

66 This study relies on two ocean high-resolution numerical simulations using the MIT general circulation  
67 model (Marshall et al., 1997). A dynamic thermodynamic sea ice model (Hibler, 1979, 1980; Zhang and  
68 Rothrock, 2000), implemented by Losch et al. (2010), is employed to simulate sea ice processes. The model  
69 domain covers the entire Arctic Ocean north of the Bering Strait and the Atlantic Ocean north of 33°S. In the  
70 horizontal, the model uses a curvilinear grid with resolutions of ~8 km (ATLARC08km) and ~4 km (AT-  
71 LARC04km). In the vertical, ATLARC08km and ATLARC04km have 50 and 100 vertical z-levels, respective-  
72 ly.

73 At the ocean surface, the model simulations are forced by momentum, heat, and freshwater fluxes comput-  
74 ed using bulk formulae and either the 6-hourly NCEP RA1 reanalysis (Kalnay et al., 1996) (ATLARC08km) or  
75 the 6-hourly ECMWF ERA-Interim reanalysis (Dee et al., 2011) (ATLARC04km). A virtual salt flux paramete-  
76 rization is used to mimic the dilution and salinification effects of rainfall, evaporation, and river discharge.  
77 The models are forced by the monthly output from the GECCO2 (Köhl, 2015) global model configuration at the  
78 open boundaries. The river runoff is applied at river mouths by a seasonal climatology. Bottom topography is  
79 derived from the ETOPO 2-min (Smith and Sandwell, 1997) database. ATLARC08km is initialized with annual  
80 mean temperature and salinity from the World Ocean Atlas 2005 (Boyer et al., 2005) and covers 1948 to 2016,  
81 and ATLARC04km starts from the initial condition of ATLARC08km at the start of the year 2002. Table 1  
82 summarizes both the simulations and their main characteristics.

83 Table 1. Summary of model simulations used in this study.

	<i>Horizontal resolution</i>	<i>Vertical grid</i>	<i>Surface forcing</i>	<i>periods</i>	<i>Output Frequency</i>
<i>ATLARC08km</i>	~8 km	50 z-levels	NCEP-RA1	1948-2016 05.01.2003- 01.12.2010	monthly daily
<i>ATLARC04km</i>	~4 km	100 z-levels	ERA-Interim	01.01.2003- 23.08.2012	daily

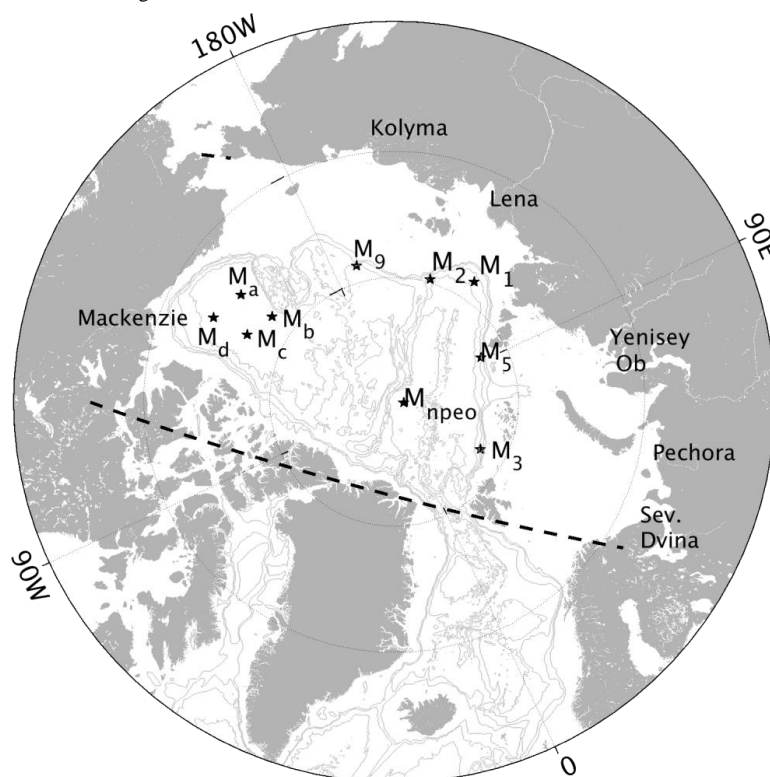
84

### 85 2.2 Satellite and in-situ observations

86 Koldunov et al. (2014) have validated ATLARC08km against tide gauge observations. We further compare  
87 the two model simulations against in-situ bottom pressure observations, GRACE observations, and satellite  
88 altimetric observations.



89 The monthly altimetric sea level observations from Armitage et al. (2016) and GRACE measurements  
 90 (Chambers and Bonin, 2012) are used in a comparison with the model simulations. For the very high-frequency  
 91 variability, bottom pressure records supplied by the Beaufort Gyre Exploration Project (BGEP,  $M_a$ ,  $M_b$ ,  $M_c$ , and  
 92  $M_d$  in Fig. 1) and the North Pole Environmental Observatory (NPEO,  $M_{npeo}$  in Fig. 1, Morison et al., 2012) are  
 93 used. Tidal signals are removed using the T\_TIDE Matlab program (Pawlowicz et al., 2002), since the model  
 94 did not include tidal forcing.



95

96 **Figure 1.** A map of the pan-Arctic Ocean presenting the locations of moorings deployed by the Nansen and  
 97 Amundsen Basin Observational System (NABOS, black pentagrams labeled with  $M_1$ ,  $M_2$ ,  $M_3$ ,  $M_5$ , and  $M_9$ ), by  
 98 the Beaufort Gyre Exploration Project (BGEP, black pentagrams marked with  $M_a$ ,  $M_b$ ,  $M_c$ ,  $M_d$ ), and by the  
 99 North Pole Environmental Observatory (NPEO, black pentagram labeled with  $M_{npeo}$ ). The black dashed lines  
 100 enclose the Arctic regions used in Section 4.2. Bathymetry contours of 500, 1000, 2000, 3000, and 4000 m are  
 101 drawn with grey lines. Main rivers are labeled with their names near the river mouths.

### 102 2.3 Relation between sea level, bottom pressure, and thermo/halosteric components

103 Following Ponte (1999) and Calafat et al. (2013), sea level anomaly  $\eta'$ , can be separated into a steric com-  
 104 ponent  $\eta'_s$  due to density change, an inverse barometer effect  $\eta'_{IB}$ , and a mass (measured by bottom pressure  
 105 observations) component  $\eta'_m$ :

$$106 \eta' = -\frac{1}{\rho_0} \int_{-H}^0 \rho' dz + \frac{1}{\rho_0 g} (\bar{P}'_a - P'_a) + \frac{1}{\rho_0 g} (P'_b - \bar{P}'_a) \quad (1)$$

107 where  $g=9.8 \text{ m s}^{-2}$  is the gravitational acceleration. The first term on the right-hand side represents the steric  
 108 effect  $\eta'_s$ , with  $\rho_0$  being a reference density ( $1025.0 \text{ kg/m}^3$  in this study) and  $\rho'$  being the density change. The



109 second term is the inverse barometer effect  $\eta'_{IB}$ :  $\bar{P}'_a$  and  $P'_a$  represent air pressure anomalies average over the  
110 global ocean and at the observing location, respectively. The last term defines the mass component  $\eta'_m$ .

111 Since the model simulations do not include the impacts of sea surface air pressure anomalies, the model-  
112 simulated sea level changes due to steric and mass components are simplified as:

$$113 \quad \eta' = -\frac{1}{\rho_0} \int_{-H}^0 \rho' dz + \frac{1}{\rho_0 g} (P'_b) \quad (2).$$

114 Separating density changes into temperature and salinity changes, we decompose the steric height  $\eta'_s$  into  
115 thermosteric height  $\eta'_{st}$  (due to temperature anomalies) and halosteric height  $\eta'_{ss}$  (due to salinity anomalies):

$$116 \quad \eta'_{st} = -\frac{1}{\rho_0} \int_{-H}^0 (\rho(T, \bar{S}, p) - \rho(\bar{T}, \bar{S}, p)) dz \quad (3),$$

$$117 \quad \eta'_{ss} = -\frac{1}{\rho_0} \int_{-H}^0 (\rho(\bar{T}, S, p) - \rho(\bar{T}, \bar{S}, p)) dz \quad (4),$$

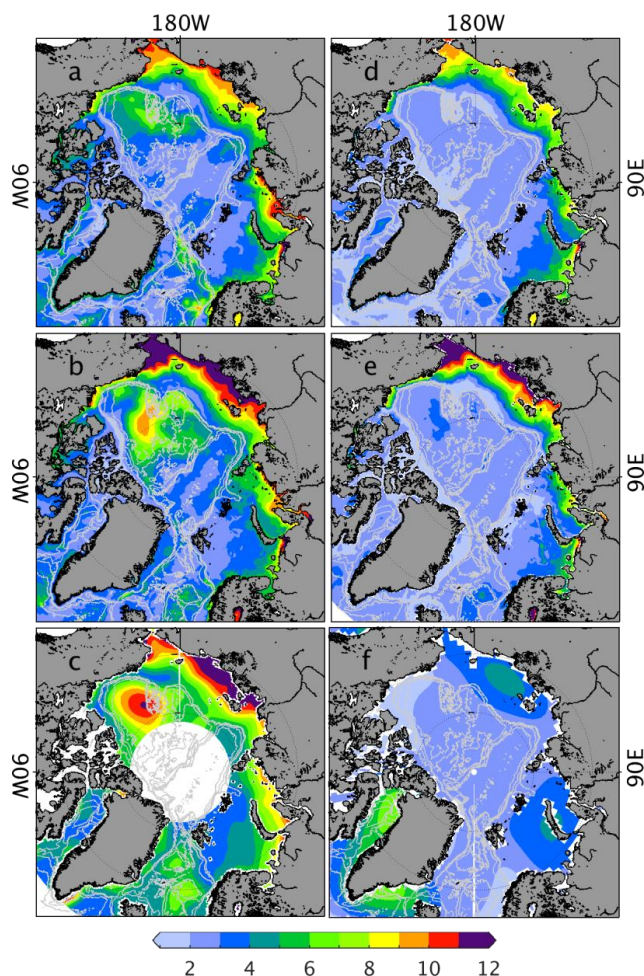
118 where  $T$ ,  $S$ , and  $p$  represent seawater temperature, salinity, and pressure. The overbars denote the average over  
119 the simulation time.

120 Before comparing the model simulation with the GRACE measurements and mooring-based bottom pres-  
121 sure observations, we remove air pressure anomalies averaged over the global ocean  $\bar{P}'_a$ , and then global-mean  
122 mass changes from GRACE-based bottom pressure observations since the virtual salt flux parameterization does  
123 not include mass transfer from land to ocean. In total, this process removes a seasonal cycle with an amplitude  
124 of  $\sim 1$ - $1.5$  cm from the measurements.

### 125 3 Testing simulations against observations

126 Koldunov et al. (2014) have demonstrated that the interannual variability of sea level in ATLARC08km and  
127 tide gauges match very well. In the present study, we further evaluate the skill of the model-simulated sea level  
128 and bottom pressure variability by comparing the root mean square (RMS) variability of sea level and bottom  
129 pressure against altimetric data (Armitage et al., 2016) and GRACE data (Chambers and Willis, 2010). In addi-  
130 tion, high-frequency bottom pressure observations from BGEP and NPEO are also compared with the two mod-  
131 el simulations.

132

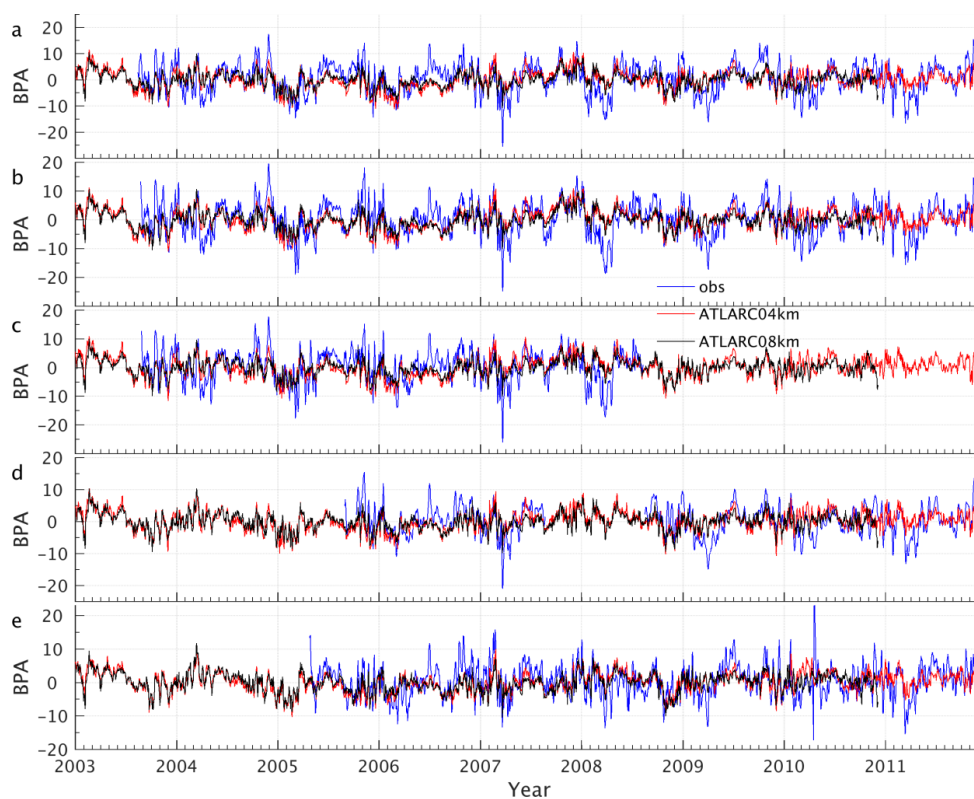


133

134 **Figure 2.** RMS variability of (a-c) sea level and (d-f) bottom pressure in (a, d) ATLARC08km, (b, e) ATLARC04km, (c)  
135 satellite altimetry, and (f) GRACE. We computed the RMS variability using monthly data from January 2003 to December  
136 2011. Bathymetry contours of 500, 1000, 2000, and 3000 m are drawn with grey lines.

137 Both the model simulations (Fig. 2a, b) and satellite altimetry (Fig. 2c) reveal pronounced sea level varia-  
138 bility in the Canadian Basin and along the coast, which could be attributed to the redistribution of water due to  
139 the shifting of basin-scale cyclonic/anticyclonic wind (Proshutinsky and Johnson, 1997) and to the discharge  
140 and transport of river runoff along the coast (Proshutinsky et al., 2007). ATLARC04km simulates more signifi-  
141 cant sea level variability than ATLARC08km, especially in the East Siberian Sea and the Canadian Basin, and  
142 matches better with the observed sea level variability. Bottom pressure also shows significant variability in the  
143 Arctic marginal seas (Fig. 2d-f), especially in the East Siberian Sea. However, due to the smoothing process  
144 applied on GRACE measurements (a 500 km Gaussian filter), both the model simulations simulate much more  
145 substantial RMS variability of bottom pressure.

146



147

148 Figure 3. Time series of bottom pressure anomalies in ATLARC08km, ATLARC04km, and in-situ observations.  
149 Observations are derived from (a) mooring A, (b) mooring B, (c) mooring C, and (d) mooring D of BGEP. Panel  
150 (e) is from the NEPO moorings. Mooring locations are marked in Fig. 1.

151 Besides monthly to decadal variability of bottom pressure, both the model simulations and the in-situ ob-  
152 servations also demonstrate significant high-frequency bottom pressure anomalies (Fig. 3). Both model simu-  
153 lations correlate well with the observations ( $\sim 0.45-0.55$ ) in the five shown locations, but ATLARC04km and  
154 ATLARC08km underestimate the RMS variability by  $\sim 30-50\%$ , with ATLARC04km showing relative more  
155 significant RMS variability.

156 The comparisons above indicate that the model simulations reproduce the observed sea level and bottom  
157 pressure variability reasonably well at both high-frequency bands and low-frequency bands. In the following  
158 parts, we will use the daily output of ATLARC04km to reveal spatial variability of sea level at high frequency  
159 and seasonal periods and use the monthly output of ATLARC08km to explore the decadal sea level variability.

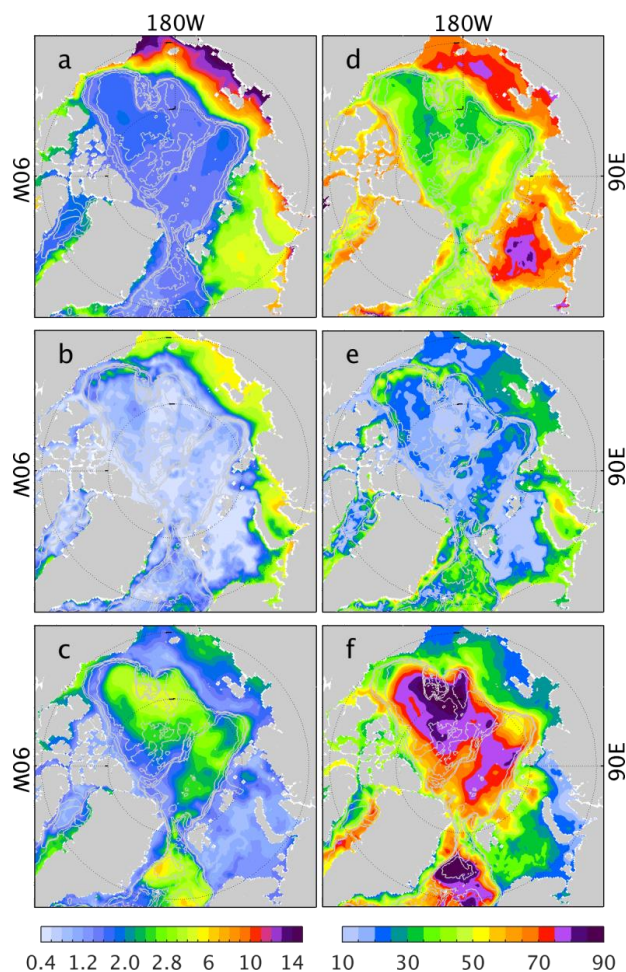
#### 160 4 Sea level variability and its relation with bottom pressure and steric height

161 A model study (Proshutinsky et al., 2007) and satellite observations (Armitage et al., 2016) showed that the  
162 Arctic sea level presents distinctive seasonal to decadal variability. In situ bottom pressure observations also  
163 reveal energetic variability at sub-monthly frequencies. Here, we concentrate on sea level variability at very  
164 high-frequency ( $<30$  days), on the seasonal cycle, and at decadal timescales ( $>4$  years).





165



166

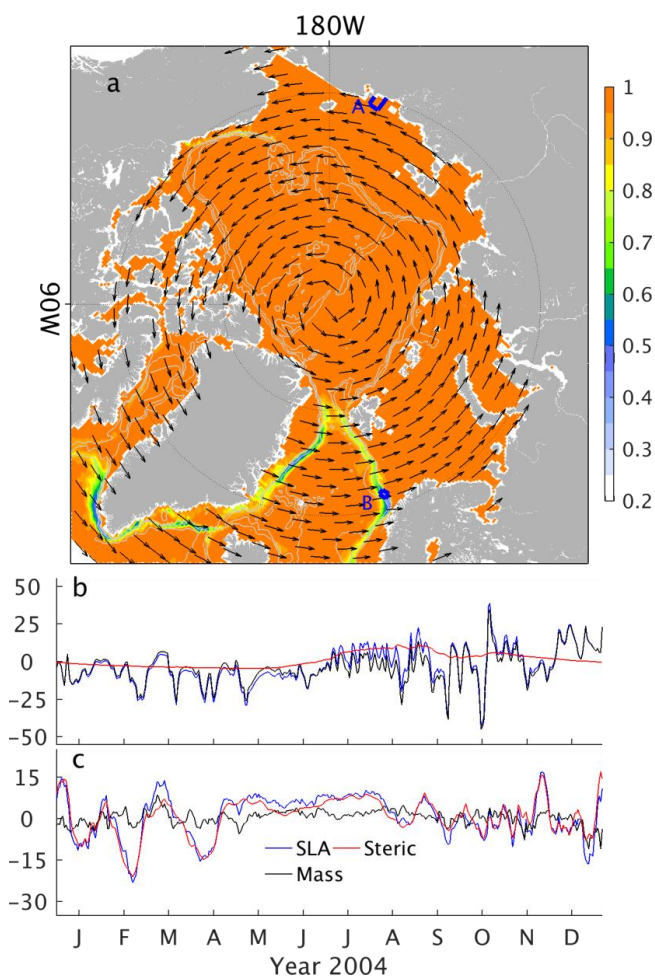
167 Figure 4. RMS variability (cm) of sea level (a) in the high-frequency band (<30 days), (b) at the seasonal cycle,  
168 and (c) at decadal periods (>4 years). Panels (d)-(f) are the corresponding ratios (%) to the total sea level vari-  
169 ance that panels (a)-(c) explained. The grey lines denote bathymetry contours of 500, 1000, 2000, and 3000 m.

170 At period <30 days, RMS variability of sea level up to 14 cm appears in the marginal seas and along the  
171 coasts (Fig. 4a), accounting for 60%~80% of the local sea level variance (Fig. 4d). The seasonal sea level varia-  
172 bility is pronounced in the marginal seas and southern edge of the Beaufort Sea, and it explains 20%-40% of the  
173 total sea level variance. In the deep regions of the pan-Arctic Ocean, the decadal variability dominates the sea  
174 level variability, and it explains more than 70%~90% of the sea level variability. Overall, in the marginal seas,  
175 sea level variability is dominated by sub-monthly and seasonal signals. In contrast, decadal sea level variability  
176 dominates in the deep regions of the pan-Arctic Ocean. Besides, seasonal variability is also visible in the south-  
177 ern periphery of the Beaufort Sea, indicating possible exchanges between the marginal seas and the Beaufort  
178 Sea.



179 **4.1 High-frequency (<30 days) variability**

180 With a coarse resolution model simulation, Vinogradova et al. (2007) demonstrated that sea level variabil-  
181 ity is coherent with and virtually equivalent to bottom pressure in the mid-latitude and subpolar regions at peri-  
182 ods <100 days, reflecting the barotropic nature of high-frequency variability (Stammer et al., 2000). Here, we  
183 revisit the high-frequency sea level variability in the pan-Arctic Ocean with high-resolution model simulations  
184 and a transfer function (Vinogradova et al., 2007) of sea level and bottom pressure.



185

186 Figure 5. (a) Amplitude (shading) and phase (black vectors) of the transfer function between sea level anomaly and bottom pressure anomaly at periods <30 days. Time series of sea level anomaly (blue lines), mass component (black lines), and steric component (red lines) averaged in (b) the East Siberian Sea (blue box A in panel a) and along (c) the NwAC (blue box B in panel a).  
187  
188  
189

190 Except for the Norwegian Atlantic Current (NwAC) and the East/West Greenland Current (EGC/WGC),  
191 the amplitude of the transfer function between sea level and mass component is ~1 (Fig. 5a) in most of the pan-



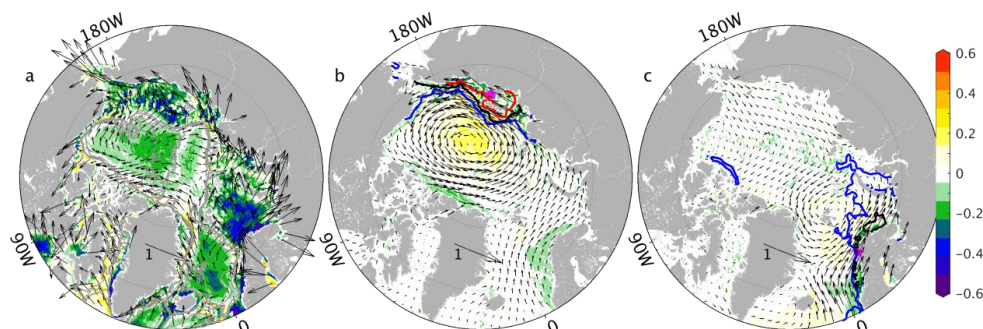
192 Arctic regions. The phases (vectors in Fig. 5a) are  $\sim 0$  in the entire Arctic Ocean, indicating that the high-  
193 frequency sea level variability is mostly barotropic. However, in the strong current regions, including NwAC,  
194 EGC, and WGC, an amplitude of the transfer function of  $\sim 0.4$  is observed, revealing that both barotropic and  
195 baroclinic processes contribute to the high-frequency sea level variability.

196 Subregions in the East Siberian Sea (A in Fig. 5a) and along the NwAC (B in Fig. 5a) are used to reveal  
197 details of the high-frequency sea level variability. It is clear that the sea level anomaly in the East Siberian Sea  
198 (Fig. 5b) is almost equivalent to the bottom pressure anomaly, and the steric component contributes slightly to  
199 the seasonal timescale. Along the NwAC (Fig. 5c), pronounced steric height variability with timescales of 20-60  
200 days is visible, which may be caused by baroclinic instability, and the mass component shows high-frequency  
201 variability.

202 The high-frequency sea level variability is mainly related to wind forcing (Fukumori et al., 1998) at high  
203 latitudes. Correlations to the wind forcing and sea level anomalies are used to explain the driving mechanisms of  
204 the high-frequency sea level variability. The negative correlations between high-frequency sea level variability  
205 and wind stress curl (shading in Fig. 6a) in the Canadian Basin and GIN seas ( $-0.3$ ) and in the marginal seas ( $-$   
206  $0.3\sim-0.5$ ) reveal that local sea level increase/decrease is partially related to convergence/divergence of Ekman  
207 transport. Positive correlations ( $0.2\sim 0.3$ ) are visible along the 1000 m isobath where strong currents exist and  
208 stratification is strong. A plausible explanation is that wind stress curl anomalies may likely result in baroclinic  
209 instabilities, resulting in the baroclinic component of sea level variability along NwAC, EGC, and WGC (e.g.,  
210 Fig. 5). In the coastal regions, the pronounced correlation of the along-shore wind stress and sea level anomaly  
211 at the high-frequency band indicates that the along-shore wind is essential to produce the significant sea level  
212 variability (vectors in Fig. 6a).

213 Correlations of sea level anomalies in regions A (Fig. 6b) and B (Fig. 6c) to the sea level anomalies  
214 (contour), wind stress (vectors), and wind stress curl (shading) demonstrate that the along-shore wind drives  
215 water towards the coast through Ekman transport which interacts with topography, rising sea level along the  
216 coast. And the sea level anomalies could propagate along the coast.

217



218

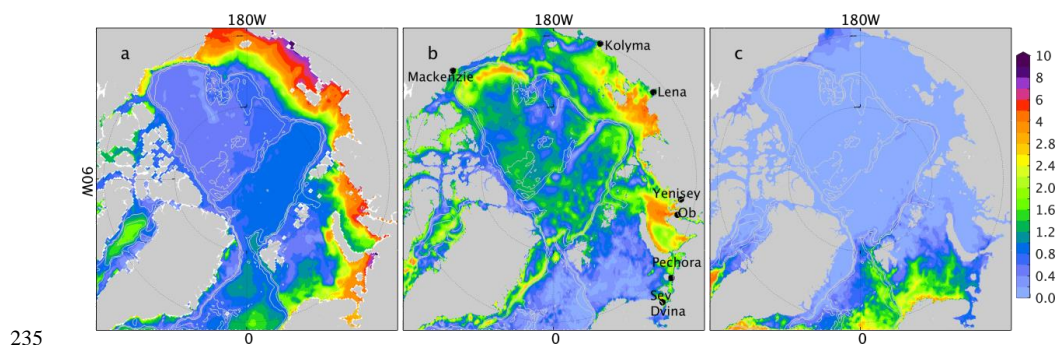
219 Figure 6. (a) Correlations of sea level anomalies to wind stress curl (shading) and wind stress (vectors) at periods  
220  $< 30$  days. Correlations of sea level anomalies in subregions of (a) the East Siberian Sea and (b) along the  
221 NwAC (see magenta pentagrams in panels (b) and (c)) to wind stress (vectors), wind stress curl (shading), and  
222 sea level anomalies (contours). The blue, black, and red contours denote correlation levels of 0.3, 0.5, and 0.7.



223 Overall, both the model simulations and the several bottom pressure records demonstrate high-frequency  
224 bottom pressure variability in the Arctic Ocean (Fig. 3). The model simulations reveal that the high-frequency  
225 variability is barotropic primarily in response to wind-induced Ekman transport and propagations of the baro-  
226 tropic signals. In the strong current regions, steric effects also contribute to local sea level variability caused  
227 by baroclinic processes.

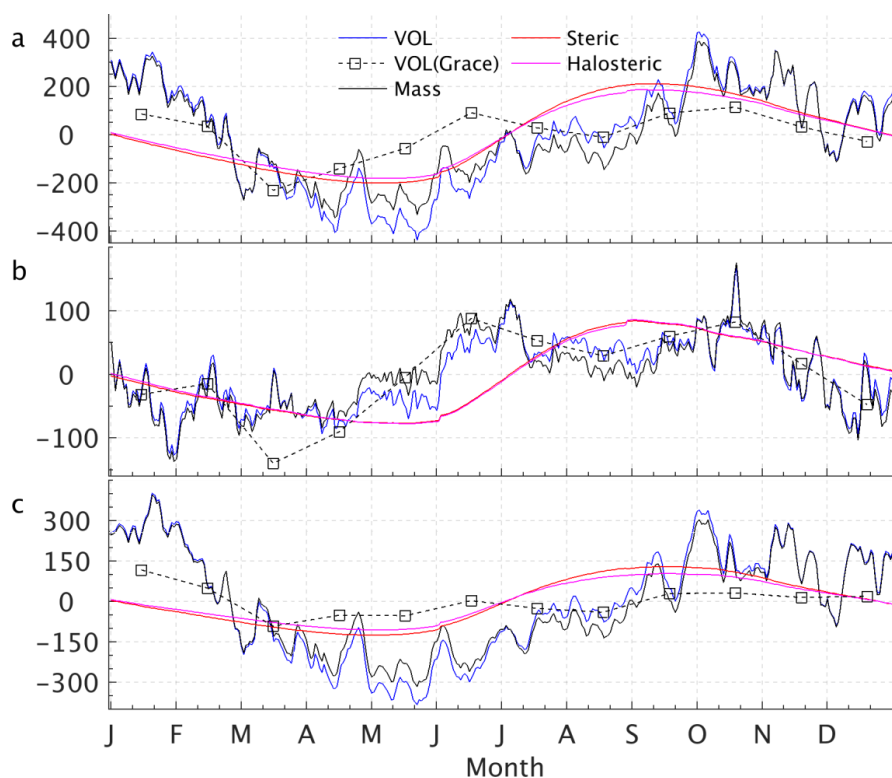
#### 228 4.2 Seasonal variability

229 Seasonal sea level variability could be related to the redistribution of water from the deep ocean to the  
230 marginal seas due to cyclonic/anticyclonic wind stress (Proshutinsky and Johnson, 1997), a seasonal variation of  
231 the Arctic Ocean volume (Armitage et al., 2016). In addition, the steric effect due to warm Atlantic inflow and  
232 sea ice formation/melting contribute to regional sea level variability in the Barents Sea (Volkov and Landerer,  
233 2013). This section focuses on the spatial-varying Arctic sea level variability at seasonal periods and its mecha-  
234 nism.



235 Figure 7. RMS variability of (a) mass, (b) halosteric, and (c) thermosteric components at the seasonal periods.

236 Like the high-frequency sea level variability, the mass component still dominates the seasonal sea level  
237 variability in the marginal seas (Fig. 4b and Fig. 7a). Halosteric effects are significant near the river mouth,  
238 seasonal ice edge, and along the coast of Alaska (Fig. 7b), indicating the spreading of freshwater driven by oce-  
239 anic flows. Pathways of freshwater from rivers and marginal seas to the Makarov Basin and to the periphery of  
240 the Beaufort Sea can also be inferred from the significant halosteric effect. The thermosteric effects dominate  
241 the ice-free region in the GIN seas and in the Barents Sea, and it is remarkably weakened as it penetrates the ice-  
242 covered Arctic Ocean (Fig. 7c).  
243



244

245 Figure 8. (a) Time series of total volume (VOL) anomaly in the Arctic Ocean (see Fig. 1 for the regions) and the  
246 contributions from mass changes (Mass) and steric effects (Steric). The halosteric component (Halosteric) and  
247 the GRACE-observed mass component are also shown. Panels (b) and (c) show the corresponding values in (b)  
248 the deep basin (>500 m) and (c) the shallow water (<500m).

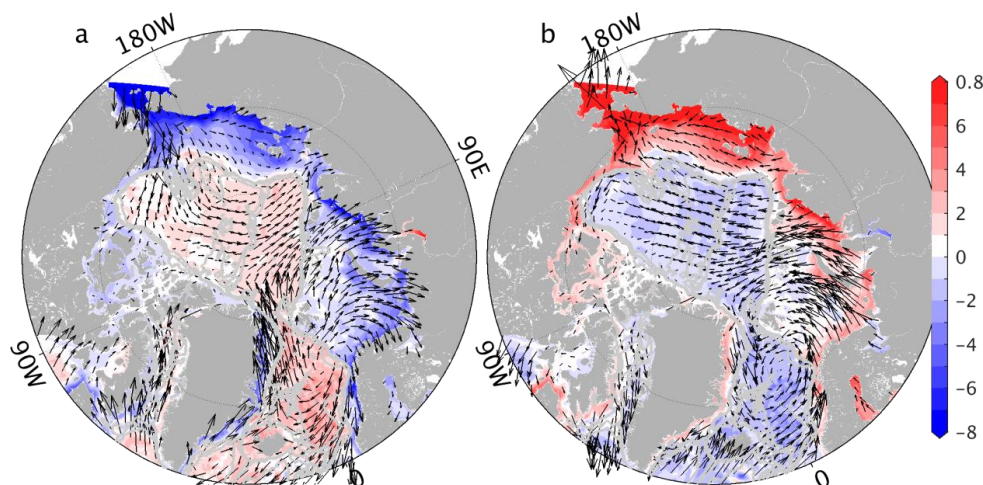
249 Sea level changes reflect total volume changes. The Arctic volume anomalies, dominated by mass compo-  
250 nent, shows a clear seasonal cycle overlaid with sub-seasonal variability (Fig. 8a). Since the surface freshwater  
251 flux is treated as a virtual salt flux, river runoff and evaporation minus precipitation do not change the total  
252 volume directly. The seasonal volume variability, especially the mass component, is driven by volume exchange-  
253 es with the Pacific and Atlantic Oceans. The steric component (red lines in Fig. 8), especially the halosteric  
254 component (magenta lines in Fig. 8), causes the volume to decrease in the winter season and increase in the  
255 summer season due to the sea ice formation/melting.

256 The model simulates more substantial seasonal mass variability than the GRACE measurement. Still, it  
257 fails to reproduce the secondary peak from May to July (Fig. 8a), which may relate to river discharge in the  
258 marginal seas. Splitting the total Arctic volume changes into contributions from the deep basin and coastal seas,  
259 we note that the secondary peak is related to volume changes in the deep basin from May to July (Fig. 8b) in  
260 both the model simulation and the GRACE observations. At the same time, volume anomalies are negative in  
261 the marginal seas. This antiphase of the volume anomalies in the deep basin and marginal seas seems to be driv-



262 en by the cyclonic/anticyclonic wind pattern in the summer/winter season (Proshutinsky and Johnson, 1997).  
263 Mean sea level anomalies from June to August (Fig. 9a) and from December to February (Fig. 9b) further reveal  
264 the antiphase of the sea level changes between the deep basin and the shallow waters. The mean pattern of wind  
265 stress anomalies (vectors in Fig. 9) indicates that wind-driven Ekman transport drives the water toward/away  
266 from the marginal seas, resulting in the antiphase of seasonal sea level variability in the deep basin and shallow  
267 waters.

268 The model simulation demonstrates the critical importance of exchanges with the Pacific and Atlantic  
269 Oceans for the Arctic volume changes at seasonal periods. The wind stress will further redistribute water in the  
270 Arctic Ocean, resulting in the antiphase pattern of sea level changes in the shallow waters and deep basin. Using  
271 a one-dimensional model, Peralta-Ferriz and Morison (2010) demonstrated that river runoff and evaporation  
272 minus precipitation (EmP) drive the basin-scale seasonal mass variation of the Arctic Ocean. This process is not  
273 included in our model simulations due to the virtual salt flux parameterization. But it should be noted that either  
274 input from river runoff and EmP (Peralta-Ferriz and Morison, 2010) or exchanges with the Pacific and Atlantic  
275 Oceans is large enough to drive the Arctic volume changes. Moreover, the wind stress will further redistribute  
276 the water to different regions. It is also expected that volume input from the rivers ( $\sim 700 \text{ km}^3$ ) could signifi-  
277 cantly alleviate the negative volume anomalies from May to August in the marginal seas.



278  
279 Figure 9. Sea level anomalies (shading) and wind stress anomalies (vectors) averaged from (a) June to August  
280 and (b) December to February.

### 281 4.3 Decadal variability

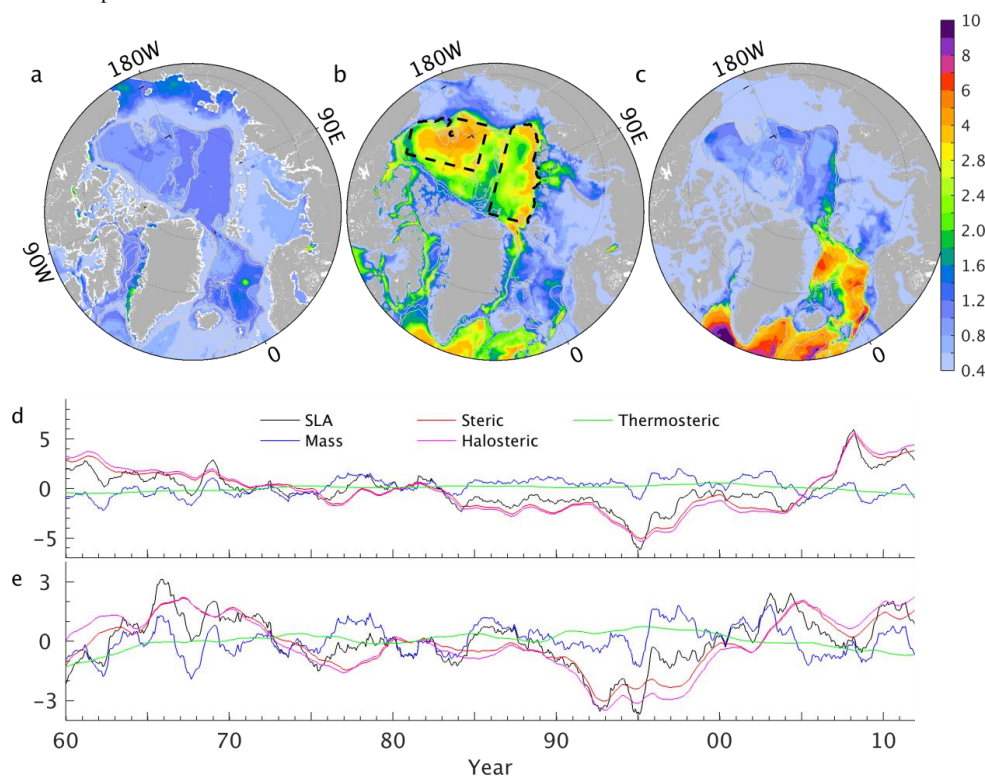
282 The Arctic sea level shows significant decadal variability driven by cyclonic/anticyclonic wind patterns  
283 (Proshutinsky and Johnson, 1997), accompanied by freshwater content changes (Häkkinen and Proshutinsky,  
284 2004; Köhl and Serra, 2014). Satellite altimetry observations were used to infer Arctic freshwater content in-  
285 creases (Armitage et al., 2016; Giles et al., 2012; Proshutinsky et al., 2019; Rose et al., 2019). This section exam-



286 ines the spatial variability of Arctic decadal sea level and addresses its relation to the mass, halosteric, and ther-  
287 mosteric components.

288 It is revealed that the pronounced decadal sea level variability in the Canadian and Eurasian Basins (Fig. 4c)  
289 is mainly due to the halosteric effect (Fig. 10b), with the mass components accounting for 20-30%. The thermo-  
290 steric effect dominates in the GIN Seas since a change from shallow convection to deep convection can lead to  
291 temperature changes of more than  $-0.2$  °C over the upper 600 m and salinity changes of 0.02 PSU over the up-  
292 per 200 m (see Fig. A1 in Brakstad et al., 2019). In the north Atlantic Ocean, the thermosteric effect dominates.  
293 At the same time, the halosteric effect compensates for the thermosteric effect, rendering more considerable  
294 thermosteric height variability than decadal total sea level variability.

295 Timeseries of sea level anomalies and its different components in Fig. 10d confirm that sea level variability  
296 in the Canadian Basin is mostly halosteric (Armitage et al., 2016; Giles et al., 2012; Morison et al., 2012), and  
297 that the thermosteric component contributes with a linear trend (not shown here). In the Eurasian Basin, the  
298 mass component, which is likely related to volume exchanges with the Atlantic Ocean and the Barents Sea, also  
299 contributes to the interannual sea level variability. The halosteric component shows clearly decadal variability  
300 and is in phase with that in the Canadian Basin. The thermosteric component slightly compensates for the halo-  
301 steric component.



302

303 Figure 10. RMS variability at the decadal period of (a) bottom pressure anomaly, (b) the halosteric component,  
304 and (c) the thermosteric component. Panels (d) and (e) show the time series of sea level anomaly and mass,



305 steric, and thermo/halosteric components in the Canadian and in the Eurasian Basins (see the regions in panel  
306 (b)), respectively. Linear trends are removed.

## 307 **5 Capability of the observing system to monitor freshwater content variability**

308 Observing Arctic freshwater content changes remains challenging (Proshutinsky et al., 2019). The results  
309 above and previous studies (Giles et al., 2012; Morison et al., 2012; Proshutinsky et al., 2019) have indicated that  
310 satellite altimetry could infer freshwater content changes. International efforts try to enhance the profiles ob-  
311 serving system, including ice-tethered profilers (ITP), shipboard observations, and moorings. Here, we test their  
312 capability to monitor the freshwater changes in an idealized setting in which 1) we do not consider influences of  
313 observational errors and 2) we assume the profiles sample the top 800 m and the moorings sample from 65-800  
314 m.

### 315 **5.1 Satellite altimetry and GRACE measurements**

316 Giles et al. (2012) used altimetric sea level observations, GRACE-based bottom pressure, and a static 1.5-  
317 layer model to infer freshwater changes in the Canadian Basin. They assumed that freshwater changes lead to  
318 sea level and isopycnal changes simultaneously, changing the layer thickness and total mass of the water col-  
319 umn. In this case, freshwater change in the water column is estimated as follows:

$$320 \Delta FW = \frac{S_2 - S_1}{S_2} \cdot \Delta h = \frac{S_2 - S_1}{S_2} \cdot \left( \eta' \cdot \left( 1 + \frac{\rho_1}{\rho_2 - \rho_1} \right) - \frac{\Delta m}{\rho_2 - \rho_1} \right) \quad (5),$$

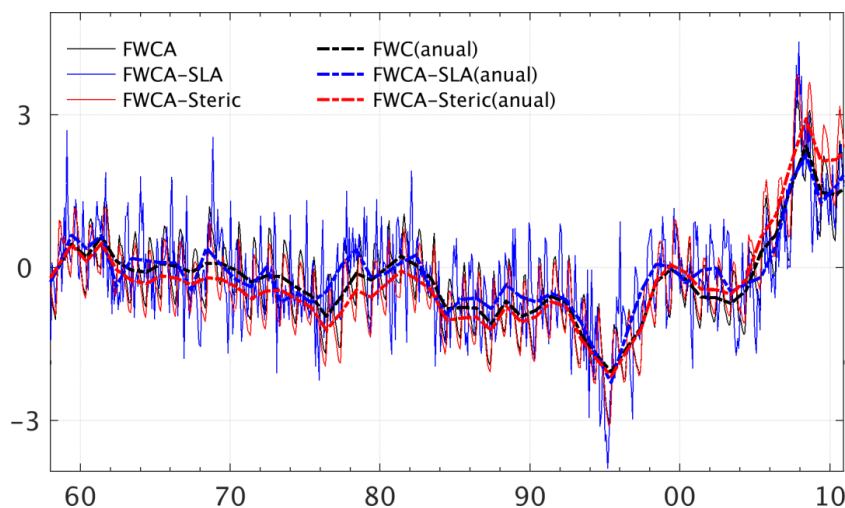
321 where  $\rho_1 = 1025.0 \text{ kg m}^{-3}$  and  $\rho_2 = 1028.0 \text{ kg m}^{-3}$  are the mean density in the top and bottom layers.  $S_1 = 33.0 \text{ PSU}$   
322 is the mean salinity in the top layer, and  $S_2 = 34.8 \text{ PSU}$  is a reference salinity.  $\eta'$  and  $\Delta m$  are the sea level anoma-  
323 ly and bottom pressure anomalies observations. Morison et al. (2012) suggest that freshwater changes depends  
324 on steric height changes linearly and could be approximated by:

$$325 \Delta FW = \alpha \cdot \eta'_s \quad (6),$$

326 where  $\alpha$  is an empirical constant estimated from in-situ profile observations and is set to 35.6.

327 As shown in Fig. 11, freshwater content changes and the two estimates show similar decadal variabilities,  
328 but differences remain in the seasonal and long-term trends. Since the halosteric effect dominates the steric  
329 effect, estimation using Eq. (6) matches the seasonal freshwater cycle very well (red and black lines), consider-  
330 ing the amplitude and phase. However, it overestimates the long-term trend (the difference between the black  
331 and red dashed lines) since Eq. (6) attributes thermosteric effect (mainly a linear trend) to freshwater changes.  
332 Eq. (5) infers a much more substantial seasonal variability of freshwater content, and the phase does not always  
333 match the real freshwater content changes (blue and black lines).





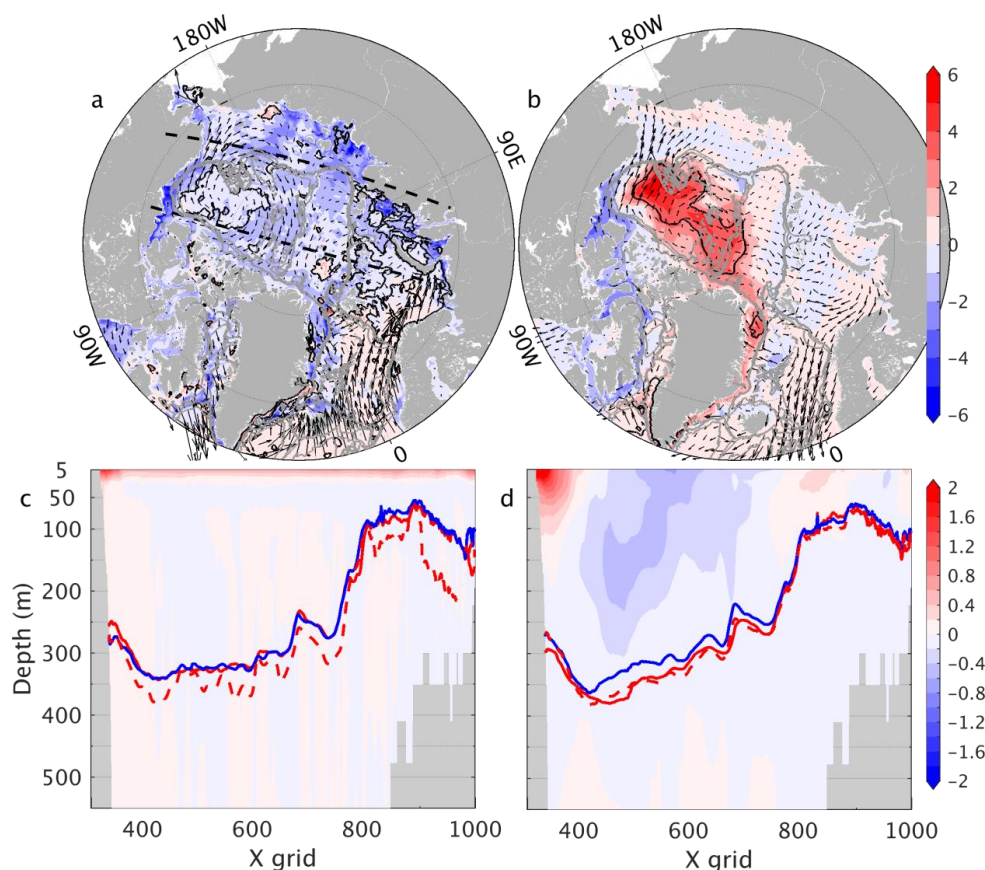
334

335 Figure 11. Freshwater content anomalies ( $10^3 \text{ km}^3$ ) and approximated based on Eq. (5) in blue and Eq. (6) in red  
 336 using the monthly output. The thick dashed lines are the annual mean values.

337 Eq. (5) assumes the isopycnal adjusts simultaneously with sea level anomaly, which may not apply in the  
 338 presence of baroclinic effects. In order to illustrate the limitation of Eq. (5) we take the differences between Feb.  
 339 2003 and Sep. 2002 (in which Eq. (5) fails to reproduce the phase and the amplitude of freshwater content  
 340 changes) and between 1994-1996 and 2008-2010 (when Eq. (5) reproduces the freshwater changes well).

341 From Sep. 2002 to Feb. 2003 (Fig. 12a), anticyclonic wind stress anomalies occur in the Beaufort Sea, re-  
 342 sulting in positive SLA through Ekman transport. However, freshwater content is reduced during this period.  
 343 The salinity difference averaged over the central Arctic Ocean reveals that salinity increases in the top 30 m  
 344 caused by ice formation. At the same time, the isopycnal ( $27.9 \text{ kg m}^{-3}$ ) does not deepen (Fig. 12c) as predicted  
 345 by Eq. (5). The assumption that freshwater content changes are captured by freshwater column thickness chang-  
 346 es  $\eta \cdot \left(1 + \frac{\rho_1}{\rho_2 - \rho_1}\right)$  (red dashed lines in Fig. 12c) fails to infer freshwater content changes in this case.

347 From 1994-1996 to 2008-2010, anticyclonic wind stress anomalies appear in the Canadian Basin, accom-  
 348 panied by positive SLA and freshwater content anomalies (Fig. 12b). During that period, Ekman pumping deep-  
 349 ens the isopycnals (blue and red lines in Fig. 12), accumulating more freshwater and reducing the local salinity  
 350 over the top 300 m (Fig. 12d). In this scenario, the water column thickness change dominates the freshwater  
 351 content variability, which is approximated by  $\eta \cdot \left(1 + \frac{\rho_1}{\rho_2 - \rho_1}\right)$  (red dashed lines in Fig. 12d). Therefore, Eq. (5)  
 352 captures the interannual freshwater content changes using the satellite altimetry observations. Therefore, caution  
 353 needs to be taken when inferring Arctic Ocean freshwater content changes using satellite altimetry observations  
 354 and GRACE measurements. In addition, Figs. 12b and 12c also indicate that Eq. (5) can be only used in the  
 355 deep basin of the Canadian Basin where wind drives the sea level changes and the deepening/shoaling of the  
 356 isopycnals.



357  
358 Figure 12. The differences of freshwater content (shading), sea level anomaly (0.15 m contour, black lines), and  
359 wind stress(vectors) between (a) Feb. 2003 and Sep. 2002, (b) 1994-1996 and 2008-2010. Panels (c) and (d) are  
360 the corresponding salinity differences (shading) average over the central Arctic Ocean (black dashed lines in  
361 panel (a)). The blue lines denote the  $27.9 \text{ kg m}^{-3}$  isopycnal in Sep. 2002 and 1994-1996. The red lines and red  
362 dashed lines are the  $27.9 \text{ kg m}^{-3}$  isopycnal and the diagnosed lines with SLA and Eq. (5) in Feb. 2003 and 2008-  
363 2010.

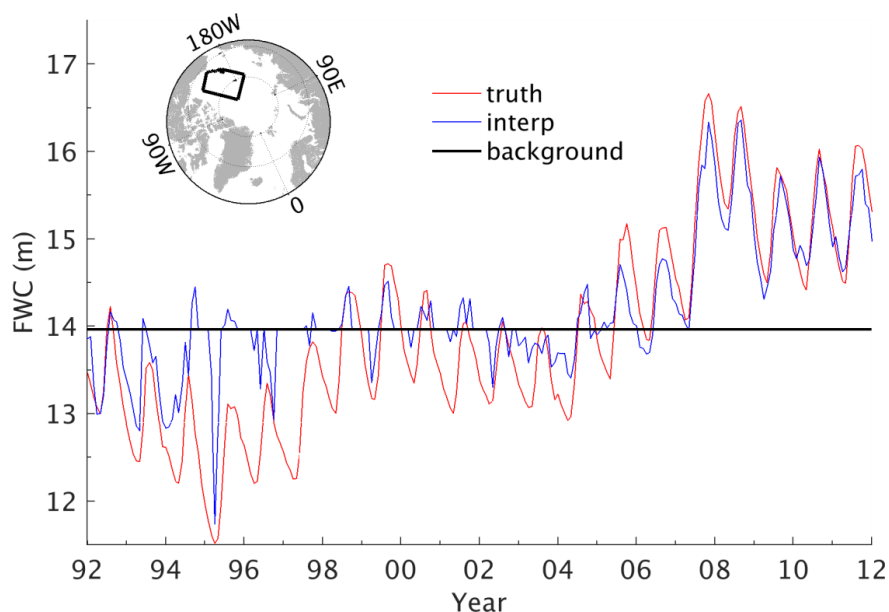
## 364 5.2 In-situ profilers

365 In-situ profilers measure salinity directly, but they are limited by sea ice presence. The endeavor of polar  
366 expeditions and the evolving measurement techniques (e.g., ITP) have generated a large number of hydrograph-  
367 ic data in the central Arctic and subarctic seas (e.g., Behrendt et al., 2018). This section examines to what extent  
368 existing hydrographic observations could help reveal Arctic freshwater content changes and identify observa-  
369 tional gaps. Based on the spatiotemporal distribution of profiles in the study of Behrendt et al. (2018) and an  
370 ensemble optimal interpolation (EnOI) scheme (Evensen, 2003;Lyu et al., 2014), we test to what extent existing  
371 profiles could help to reconstruct the "true" state (here the ATLARC08km simulation) during the periods 1992  
372 to 2012. Details of the EnOI scheme are given in Appendix A.

373

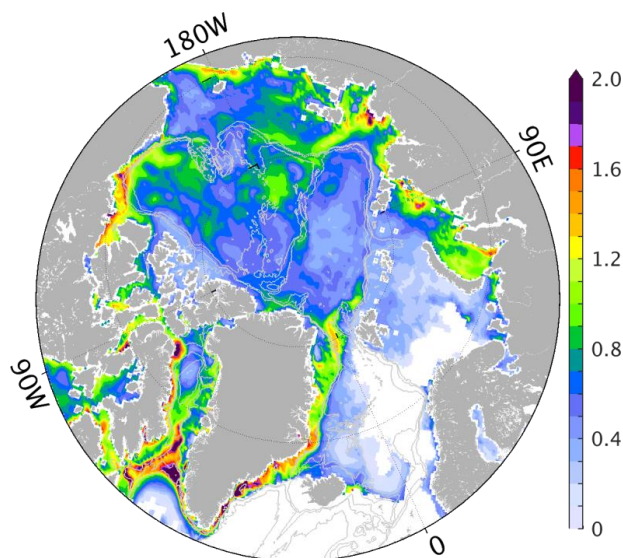


374



375 Figure 13. Mean freshwater content (in meter) in the Canadian Basin (enclosed by the black line in the top sub-  
376 plot) from the background state, the "truth", and the optimal interpolation reconstructed state (see legend).

377 As shown in Fig. 13, the sparse in-situ profiles help bring the freshwater content in the background state  
378 close to the "truth" state. However, it is not until 2007 that the reconstructed state reproduces the seasonal to  
379 inter-annual freshwater content variability in the Canadian Basin, benefiting from the increasing number of  
380 research activities and international collaborations. In Fig. 14, we further examined RMS errors of freshwater  
381 content depending on geographic locations from 2007 to 2012. Besides the Barents Sea, more significant errors  
382 remain in coastal areas due to the lacking of in-situ profiles. In the Laptev Sea and the Alaska coast, we note  
383 pronounced errors extending from the coasts to the deep basin, underlining the observing requirements.



384

385 Figure 14. Root mean square errors of freshwater content between the reconstructed state and the "truth".

386 The above results highlight that the increase of hydrographic observations have enhanced our ability to re-  
387 construct the Arctic freshwater content changes since 2007. A lack of hydrographic observations in the coastal  
388 areas results in significant errors in the marginal seas, which require extensive international collaborations.

## 389 6 Summary and conclusions

390 Sea level variability reflects changes in ocean dynamics, atmospheric forcing, and terrestrial runoff pro-  
391 cesses (Stammer et al., 2013). In particular, sea level observations have been applied to infer freshwater content  
392 changes (Armitage et al., 2016; Giles et al., 2012; Proshutinsky et al., 2019) in the central Arctic Ocean. To com-  
393 plement our understanding of the Arctic sea level variability and its mechanisms, we use two high-resolution  
394 ATLARC model simulations to investigate the Arctic sea level variability at different timescales and the relation  
395 with bottom pressure and thermo/halosteric effects, identifying critical observational gaps that need to be filled.

396 Both the model simulations and mooring observations reveal very high-frequency bottom pressure varia-  
397 tions. The model simulations confirm that the bottom pressure anomaly is equivalent to sea level anomaly in  
398 most areas of the Arctic Ocean at periods <30 days, reflecting the barotropic nature of this high-frequency vari-  
399 ability. Correlation analyses show that the high-frequency sea level variability is caused by wind-driven Ekman  
400 transport and propagations of these barotropic signals.

401 The seasonal sea level variability is dominated by volume exchanges with the Pacific and Atlantic Oceans  
402 and the redistribution of the water by wind stress. Halosteric effects due to river runoff and ice melt-  
403 ing/formation are also pronounced in the marginal seas and seasonal sea ice extent regions. Peralta-Ferriz and  
404 Morison (2010) demonstrated that river runoff and EmP drive the seasonal cycle of the Arctic bottom pressure.  
405 Although the virtual salt flux parameterization could not mimic the influences of volume input from rivers and  
406 surface fluxes, the model simulations still simulate much stronger seasonal mass anomalies than the observa-



407 tions from GRACE. Either volume exchanges with the Pacific and Atlantic Oceans or volume input from river  
408 runoff and EmP are large enough to cause the Arctic Ocean's seasonal volume variability. They should work  
409 together, resulting in the Arctic seasonal volume variability. We speculate that using river runoff and EmP as  
410 volume flux, rather than the virtual salt flux, could likely improve the volume and sea level variability in the  
411 marginal seas from April to July, since the volume inputs from river runoff could alleviate the negative volume  
412 anomalies in the marginal seas caused by wind.

413 At decadal timescales, the model simulations further confirm that the pronounced sea level variability in the  
414 central Arctic Ocean, especially in the Canadian Basin, is mainly a halosteric effect. Using the satellite altimet-  
415 ric observations and GRACE observations, the method of Giles et al. (2012) could infer the freshwater content  
416 changes in the Canadian Basin very well at timescales longer than one year since isopycnal requires time to  
417 adjust to sea level changes. Inferring freshwater content changes using a linear relation of freshwater content  
418 and steric height (Morison et al., 2012) reveals both the interannual and the seasonal variability of freshwater  
419 content. However, cautions need to be taken since the method also attributes the thermosteric effects to haloster-  
420 ic effects, resulting in an additional linear trend. In addition, uncertainties in the satellite altimetric and GRACE  
421 measurements make the estimation more complicated and introduce significant uncertainties in the steric effects  
422 and freshwater content estimation (Ludwigsen and Andersen, 2021).

423 The increasing number of international collaborations and new measurement techniques have generat-  
424 ed a large number of profiles. From reconstructing the salinity with synthetic observations, we note that the in-  
425 situ profile system seems to capture the seasonal freshwater variability since the year 2007, encouraging further  
426 Arctic data synthesis studies (Behrendt et al., 2018; Cheng and Zhu, 2016; Steele et al., 2001) with more compli-  
427 cated interpolation methods. In addition, international collaborations need to be enhanced to fill in the observa-  
428 tional gaps in the marginal seas. Further, observing system simulation experiments (e.g., Lyu et al.,  
429 2021; Nguyen et al., 2020) should be performed coordinately to develop an autonomous observing system in the  
430 Arctic Ocean.

#### 431 **7 Data availability**

432 The data used to create the plots in the paper are available at Pangaea (<https://issues.pangaea.de/browse/PDI-22940>). To access results of the two high resolution ATLARC model simulations, please contact Dr. Nuno Serra  
433 at <https://www.ifm.uni-hamburg.de/en/institute/staff/serra.html>. Observational data were retrieved from publicly  
434 available sources and are listed in the text.  
435

436

437 *Author contribution.* G. Lyu performed the analysis and wrote the paper. N. Serra performed the model simula-  
438 tions. D. Stammer proposed this study and M. Zhou provided advice on the analysis.

439 *Competing interests.* The authors declare that they have no conflict of interest.

440



## 441 Acknowledgments

442 This work was supported partly through funding received from project INTAROS, funded by the European  
443 Union (Grant No. 727890). G. Lyu and M. Zhou also thank the support from project STRESSOR, funded by the  
444 National Natural Science Foundation of China (Grant No. 41861134040). We thank ECMWF and NCEP for  
445 offering, respectively, the ERAInterim and NCEP-RA1 atmospheric reanalysis data. We also thank NASA,  
446 BGEP, NPEO, and NABOS for supplying observational data used in the model validation. All model simula-  
447 tions were performed at the Deutsches Klimarechenzentrum (DKRZ), Hamburg, Germany. Contribution to the  
448 DFG funded Excellence Cluster CLICCS at the Center für Erdsystemforschung und Nachhaltigkeit (CEN) of  
449 Universität Hamburg.

## 450 Appendix A

### 451 An EnOI Scheme

452 We use an EnOI scheme (Cheng and Zhu, 2016) to reconstruct the salinity in the Arctic Ocean using syn-  
453 thetic observations. The analysis state  $\varphi^a$  is a linear combination of a background field  $\varphi^f$  and in-situ observa-  
454 tions  $d$ :

$$455 \varphi^a = \varphi^f + K(d - H\varphi^f) \quad (\text{A1}),$$

456 where  $H$  is a transfer matrix that maps model state from model space to observation space. In this study, the  
457 background field of salinity  $\varphi^f$  is taken as the mean salinity over the period 1992-2012.  $K$  is the Kalman gain,  
458 calculated as:

$$459 K = A' A'^T H^T (H A' A'^T H^T + \gamma \gamma^T)^{-1} \quad (\text{A2}).$$

460 The superscript  $T$  denotes matrix transposition. In this formulation, we use  $A'$ , the salinity deviation from  
461 the mean salinity, to compute the error covariance of the background state ( $A' A'^T$ ). We use monthly data from  
462 the year 1992 to 2012 to compute  $A'$ , resulting in a total of 252 ensemble members. For simplicity, we assume  
463 the observational errors  $\gamma$  only depend on depth, ranging from 0.09 PSU at the surface to 0.02 PSU in the deep  
464 ocean, and are not correlated.

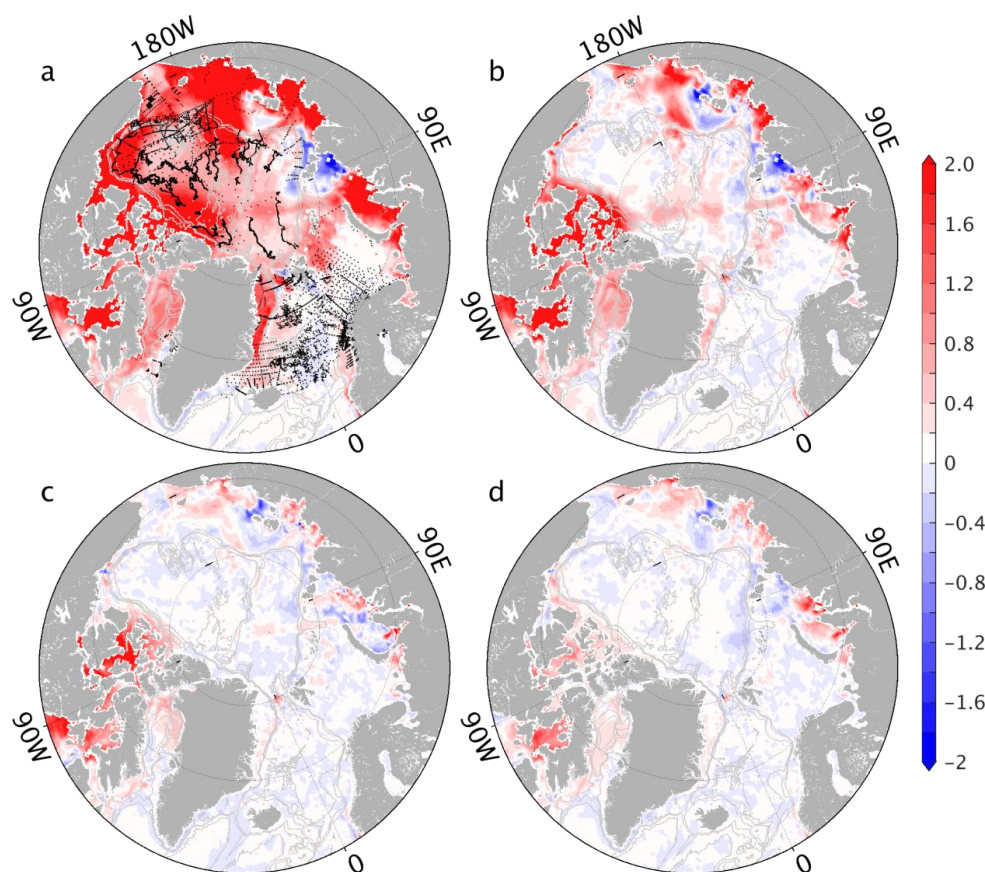
465 The use of ensemble members to approximate the background error covariance ( $A' A'^T$ ) will inevitably  
466 introduce long-distance correlations and propagate the observational information incorrectly over a much longer  
467 distance. Therefore, we introduce a Gaussian filter as a function of the distance between observational locations  
468 and the model grid and an influencing radius to ensure that only observations within the influencing radius of a  
469 model grid point could modify the analysis state.

470 Taken the "true" salinity state from August 1992 and observation locations from the year 2008 (black dots  
471 in Fig. A1a), we test the impacts of the influencing radius on the analysis field. The background state is more  
472 saline than the truth (Fig. A1a). With a 300 km influencing radius (Fig. A1b), the analysis state reduces the  
473 errors near the observations while significant errors remain in regions far away from observations. Increasing  
474 the influencing radius to 1000 km, we see that salinity errors in the marginal seas, north pole areas and the  
475 Baffin bay are reduced (Fig. A1c). A 2400 km influencing radius further reduces salinity error in the Canadian



476 Arctic Archipelago (Fig. A1d). However, only slight improvements are observed in the central Arctic Ocean,  
477 and errors in the Kara Sea are slightly increased. Since we focus on the Arctic freshwater content variability,  
478 we use a 1000 km influencing radius throughout this study.

479



480

481 Figure A1. Example of sea surface salinity difference between (a) the background and the truth, (b) the analysis  
482 with an influencing radius of 300 km and the truth, (c) the analysis with an influencing radius of 1000 km and  
483 the truth, and (d) the analysis with an influencing radius of 2400 km and the “truth”. Black dots in panel (a)  
484 denote the locations of synthetic observations, sampled using sites of the observations from year 2008.

#### 485 References

486 AMAP, 2019. AMAP Climate Change Update 2019: An Update to Key Findings of Snow, Water, Ice and Permafrost in the Arctic (SWIPA) 2017. Arctic Monitoring and Assessment Programme (AMAP), Oslo, Norway.  
487 12 pp.  
489 Armitage, T. W., Bacon, S., Ridout, A. L., Thomas, S. F., Aksenov, Y., and Wingham, D. J.: Arctic sea surface  
490 height variability and change from satellite radar altimetry and grace, 2003–2014, *Journal of Geophysical*  
491 *Research: Oceans*, 121, 4303-4322, 10.1002/2015JC011579, 2016.  
492 Behrendt, A., Sumata, H., Rabe, B., and Schauer, U.: Udash – unified database for arctic and subarctic  
493 hydrography, *Earth Syst. Sci. Data*, 10, 1119-1138, 10.5194/essd-10-1119-2018, 2018.



- 494 Boyer, T., Levitus, S., Garcia, H., Locarnini, R. A., Stephens, C., and Antonov, J.: Objective analyses of annual,  
495 seasonal, and monthly temperature and salinity for the world ocean on a 0.25 grid, *International Journal of*  
496 *Climatology*, 25, 931-945, 10.1002/joc.1173, 2005.
- 497 Brakstad, A., Våge, K., Håvik, L., and Moore, G. W. K.: Water mass transformation in the greenland sea during  
498 the period 1986–2016, *Journal of Physical Oceanography*, 49, 121-140, 10.1175/jpo-d-17-0273.1, 2019.
- 499 Calafat, F., Chambers, D., and Tsimplis, M.: Inter-annual to decadal sea-level variability in the coastal zones of  
500 the norwegian and siberian seas: The role of atmospheric forcing, *Journal of Geophysical Research: Oceans*,  
501 118, 1287-1301, 10.1002/jgrc.20106, 2013.
- 502 Chambers, D. P., and Willis, J. K.: A global evaluation of ocean bottom pressure from grace, omct, and steric-  
503 corrected altimetry, *Journal of Atmospheric and Oceanic Technology*, 27, 1395-1402, 10.1175/2010jtecho738.1,  
504 2010.
- 505 Chambers, D. P., and Bonin, J. A.: Evaluation of release-05 grace time-variable gravity coefficients over the  
506 ocean, *Ocean Sci.*, 8, 859-868, 10.5194/os-8-859-2012, 2012.
- 507 Cheng, L., and Zhu, J.: Benefits of cmip5 multimodel ensemble in reconstructing historical ocean subsurface  
508 temperature variations, *Journal of Climate*, 29, 5393-5416, 10.1175/jcli-d-15-0730.1, 2016.
- 509 Dee, D. P., Uppala, S., Simmons, A., Berrisford, P., Poli, P., Kobayashi, S., Andrae, U., Balmaseda, M.,  
510 Balsamo, G., and Bauer, d. P.: The era-interim reanalysis: Configuration and performance of the data  
511 assimilation system, *Quarterly Journal of the royal meteorological society*, 137, 553-597, 10.1002/qj.828, 2011.
- 512 Evensen, G.: The ensemble kalman filter: Theoretical formulation and practical implementation, *Ocean*  
513 *Dynamics*, 53, 343-367, 10.1007/s10236-003-0036-9, 2003.
- 514 Forget, G., Campin, J. M., Heimbach, P., Hill, C. N., Ponte, R. M., and Wunsch, C.: Ecco version 4: An  
515 integrated framework for non-linear inverse modeling and global ocean state estimation, *Geoscientific Model*  
516 *Development*, 8, 3071, 10.5194/gmd-8-3071-2015, 2015.
- 517 Fukumori, I., Raghunath, R., and Fu, L.-L.: Nature of global large-scale sea level variability in relation to  
518 atmospheric forcing: A modeling study, *Journal of Geophysical Research: Oceans*, 103, 5493-5512,  
519 10.1029/97JC02907, 1998.
- 520 Giles, K. A., Laxon, S. W., Ridout, A. L., Wingham, D. J., and Bacon, S.: Western arctic ocean freshwater  
521 storage increased by wind-driven spin-up of the beaufort gyre, *Nature Geoscience*, 5, 194, 10.1038/ngeo1379,  
522 2012.
- 523 Häkkinen, S., and Proshutinsky, A.: Freshwater content variability in the arctic ocean, *Journal of Geophysical*  
524 *Research: Oceans*, 109, 10.1029/2003JC001940, 2004.
- 525 Hibler, W. D.: A dynamic thermodynamic sea ice model, *Journal of Physical Oceanography*, 9, 815-846,  
526 10.1175/1520-0485(1979)009<0815:adtsim>2.0.co;2, 1979.
- 527 Hibler, W. D.: Modeling a variable thickness sea ice cover, *Monthly Weather Review*, 108, 1943-1973,  
528 10.1175/1520-0493(1980)108<1943:mavtsi>2.0.co;2, 1980.
- 529 Köhl, A., and Serra, N.: Causes of decadal changes of the freshwater content in the arctic ocean, *Journal of*  
530 *Climate*, 27, 3461-3475, 10.1175/jcli-d-13-00389.1, 2014.
- 531 Kalnay, E., Kanamitsu, M., Kistler, R., Collins, W., Deaven, D., Gandin, L., Iredell, M., Saha, S., White, G.,  
532 and Woollen, J.: The ncep/ncar 40-year reanalysis project, *Bulletin of the American meteorological Society*, 77,  
533 437-471, 10.1175/1520-0477(1996)077<0437:TNYRP>2.0.CO;2, 1996.
- 534 Koldunov, N. V., Serra, N., Köhl, A., Stammer, D., Henry, O., Cazenave, A., Prandi, P., Knudsen, P., Andersen,  
535 O. B., and Gao, Y.: Multimodel simulations of arctic ocean sea surface height variability in the period 1970–  
536 2009, *Journal of Geophysical Research: Oceans*, 119, 8936-8954, 10.1002/2014JC010170, 2014.
- 537 Llovel, W., Willis, J. K., Landerer, F. W., and Fukumori, I.: Deep-ocean contribution to sea level and energy  
538 budget not detectable over the past decade, *Nature Climate Change*, 4, 1031-1035, 10.1038/nclimate2387, 2014.
- 539 Losch, M., Menemenlis, D., Campin, J.-M., Heimbach, P., and Hill, C.: On the formulation of sea-ice models.  
540 Part 1: Effects of different solver implementations and parameterizations, *Ocean Modelling*, 33, 129-144,  
541 10.1016/j.ocemod.2009.12.008, 2010.
- 542 Ludwigsen, C. A., and Andersen, O. B.: Contributions to arctic sea level from 2003 to 2015, *Advances in Space*  
543 *Research*, 68, 703-710, 10.1016/j.asr.2019.12.027, 2021.





- 544 Lyu, G., Wang, H., Zhu, J., Wang, D., Xie, J., and Liu, G.: Assimilating the along-track sea level anomaly into  
545 the regional ocean modeling system using the ensemble optimal interpolation, *Acta Oceanologica Sinica*, 33,  
546 72–82, 10.1007/s13131-014-0469-7, 2014.
- 547 Lyu, G., Koehl, A., Serra, N., and Stammer, D.: Assessing the current and future arctic ocean observing system  
548 with observing system simulating experiments, *Quarterly Journal of the Royal Meteorological Society*, n/a, 1–21,  
549 10.1002/qj.4044, 2021.
- 550 Marshall, J., Adcroft, A., Hill, C., Perelman, L., and Heisey, C.: A finite-volume, incompressible navier stokes  
551 model for studies of the ocean on parallel computers, *Journal of Geophysical Research: Oceans*, 102, 5753–5766,  
552 10.1029/96JC02775, 1997.
- 553 Morison, J., Kwok, R., Peralta-Ferriz, C., Alkire, M., Rigor, I., Andersen, R., and Steele, M.: Changing arctic  
554 ocean freshwater pathways, *Nature*, 481, 66, 10.1038/nature10705, 2012.
- 555 Nguyen, A. T., Heimbach, P., Garg, V. V., Ocaña, V., Lee, C., and Rainville, L.: Impact of synthetic arctic argo-  
556 type floats in a coupled ocean–sea ice state estimation framework, *Journal of Atmospheric and Oceanic  
557 Technology*, 37, 1477–1495, 10.1175/jtech-d-19-0159.1, 2020.
- 558 Overland, J. E., Ballinger, T. J., Cohen, J., Francis, J. A., Hanna, E., Jaiser, R., Kim, B. M., Kim, S. J., Ukita, J.,  
559 Vihma, T., Wang, M., and Zhang, X.: How do intermittency and simultaneous processes obfuscate the arctic  
560 influence on midlatitude winter extreme weather events?, *Environmental Research Letters*, 16, 043002,  
561 10.1088/1748-9326/abdb5d, 2021.
- 562 Pawlowicz, R., Beardsley, B., and Lentz, S.: Classical tidal harmonic analysis including error estimates in  
563 matlab using `t_tide`, *Computers & Geosciences*, 28, 929–937, 10.1016/S0098-3004(02)00013-4, 2002.
- 564 Peralta-Ferriz, C., and Morison, J.: Understanding the annual cycle of the arctic ocean bottom pressure,  
565 *Geophysical Research Letters*, 37, 10.1029/2010gl042827, 2010.
- 566 Perovich, D., Meier, W., Tschudi, M., Hendricks, S., Petty, A., Divine, D., Farrell, S., Gerland, S., Haas, C., and  
567 Kaleschke, L.: Arctic report card 2020: Sea ice, 2020.
- 568 Polyakov, I. V., Pnyushkov, A. V., Alkire, M. B., Ashik, I. M., Baumann, T. M., Carmack, E. C., Goszczko, I.,  
569 Guthrie, J., Ivanov, V. V., Kanzow, T., Krishfield, R., Kwok, R., Sundfjord, A., Morison, J., Rember, R., and  
570 Yulin, A.: Greater role for atlantic inflows on sea-ice loss in the eurasian basin of the arctic ocean, *Science*, 356,  
571 285–291, 10.1126/science.aai8204, 2017.
- 572 Ponte, R. M.: A preliminary model study of the large-scale seasonal cycle in bottom pressure over the global  
573 ocean, *Journal of Geophysical Research: Oceans*, 104, 1289–1300, 10.1029/1998JC900028, 1999.
- 574 Proshutinsky, A., Bourke, R., and McLaughlin, F.: The role of the beaufort gyre in arctic climate variability:  
575 Seasonal to decadal climate scales, *Geophysical Research Letters*, 29, 10.1029/2002GL015847, 2002.
- 576 Proshutinsky, A., Ashik, I., Häkkinen, S., Hunke, E., Krishfield, R., Maltrud, M., Maslowski, W., and Zhang, J.:  
577 Sea level variability in the arctic ocean from aomip models, *J Geophys Res-Oceans*, 112,  
578 10.1029/2006jc003916, 2007.
- 579 Proshutinsky, A., Krishfield, R., Toole, J. M., Timmermans, M.-L., Williams, W., Zimmermann, S., Yamamoto-  
580 Kawai, M., Armitage, T. W. K., Dukhovskoy, D., Golubeva, E., Manucharyan, G. E., Platov, G., Watanabe, E.,  
581 Kikuchi, T., Nishino, S., Itoh, M., Kang, S.-H., Cho, K.-H., Tateyama, K., and Zhao, J.: Analysis of the beaufort  
582 gyre freshwater content in 2003–2018, *Journal of Geophysical Research: Oceans*, 124, 9658–9689,  
583 10.1029/2019jc015281, 2019.
- 584 Proshutinsky, A. Y., and Johnson, M. A.: Two circulation regimes of the wind-driven arctic ocean, *Journal of  
585 Geophysical Research: Oceans*, 102, 12493–12514, 10.1029/97JC00738, 1997.
- 586 Rose, S. K., Andersen, O. B., Passaro, M., Ludwigsen, C. A., and Schwatke, C.: Arctic ocean sea level record  
587 from the complete radar altimetry era: 1991–2018, *Remote Sensing*, 11, 1672, 10.3390/rs11141672, 2019.
- 588 Smith, W. H. F., and Sandwell, D. T.: Global sea floor topography from satellite altimetry and ship depth  
589 soundings, *Science*, 277, 1956–1962, 10.1126/science.277.5334.1956, 1997.
- 590 Stammer, D., Wunsch, C., and Ponte, R. M.: De-aliasing of global high frequency barotropic motions in  
591 altimeter observations, *Geophysical Research Letters*, 27, 1175–1178, 10.1029/1999gl011263, 2000.
- 592 Stammer, D., Cazenave, A., Ponte, R. M., and Tamisiea, M. E.: Causes for contemporary regional sea level  
593 changes, *Annual Review of Marine Science*, 5, 21–46, 10.1146/annurev-marine-121211-172406, 2013.



- 594 Steele, M., Morley, R., and Ermold, W.: Phc: A global ocean hydrography with a high-quality arctic ocean,  
595 Journal of Climate, 14, 2079-2087, 10.1175/1520-0442(2001)014<2079:pagoHW>2.0.CO;2, 2001.
- 596 Vinogradova, N. T., Ponte, R. M., and Stammer, D.: Relation between sea level and bottom pressure and the  
597 vertical dependence of oceanic variability, Geophysical research letters, 34, 10.1029/2006GL028588, 2007.
- 598 Volkov, D. L., and Landerer, F. W.: Nonseasonal fluctuations of the arctic ocean mass observed by the grace  
599 satellites, Journal of Geophysical Research: Oceans, 118, 6451-6460, 10.1002/2013JC009341, 2013.
- 600 Volkov, D. L., Landerer, F. W., and Kirillov, S. A.: The genesis of sea level variability in the barents sea,  
601 Continental Shelf Research, 66, 92-104, 10.1016/j.csr.2013.07.007, 2013.
- 602 Woodgate, R. A., Weingartner, T. J., and Lindsay, R.: Observed increases in bering strait oceanic fluxes from  
603 the pacific to the arctic from 2001 to 2011 and their impacts on the arctic ocean water column, Geophysical  
604 Research Letters, 39, 10.1029/2012GL054092, 2012.
- 605 Zhang, J., and Rothrock, D. A.: Modeling arctic sea ice with an efficient plastic solution, Journal of Geophysical  
606 Research: Oceans, 105, 3325-3338, 10.1029/1999JC900320, 2000.
- 607
- 608